*remote sensing*

MDPI

*Article*

# Joint Transmit Waveform and Receive Mismatched Filter Design to Suppress Range Sidelobe

**Hairui Wang *, Haihong Tao, Tiantian Zhong and Wendi Li**

The National Key Laboratory of Radar Signal Processing, Xidian University, Xi'an 710071, China; hhtao@xidian.edu.cn (H.T.); ttzhong@stu.xidian.edu.cn (T.Z.); 23021110305@stu.xidian.edu.cn (W.L.)
* Correspondence: wanghairui@stu.xidian.edu.cn

**Abstract:** Pulse compression technology can augment the likelihood of target discernment without degradation and without amplifying system hardware requisites. However, radar-communication integrated waveforms may cause mismatches in reception due to communication modulation, leading to increased loss in processing gain (LPG). This method aims to achieve communication transmission while suppressing near-range sidelobe interference (NRSI) with a minor sacrifice in LPG. An environment-based weighted mismatched filter (EWMF) design methodology is proposed to attenuate NRSI to the requisite level, with further control of LPG possible by adjusting communication modulation parameters. Moreover, the alternating direction method of multipliers is employed to jointly optimize the integrated waveform and filter design. The effectiveness of this method is demonstrated using the average sidelobe level over a specified region as the performance metric. Theoretical evaluation and experimental results confirm the applicability of waveforms using EWMF, effectively suppressing NRSI, and this method is suitable for all waveforms based on pulse compression processing. Notably, it offers cost-reduction advantages without requiring modifications to the radar transmitter or receiver.

**Keywords:** radar-communication integrated waveform; mismatched filter; loss in processing gain (LPG); alternating direction method of multipliers (ADMM)

check for updates

Academic Editor: Piotr Samczynski

Received: 11 November 2024
Revised: 20 December 2024
Accepted: 3 January 2025
Published: 7 January 2025

**Citation:** Wang, H.; Tao, H.; Zhong, T.; Li, W. Joint Transmit Waveform and Receive Mismatched Filter Design to Suppress Range Sidelobe. *Remote Sens.* **2025**, *17*, 175. https://doi.org/10.3390/rs17020175

**Copyright:** © 2025 by the authors. Licensee MDPI, Basel, Switzerland. This article is an open access article distributed under the terms and conditions of the Creative Commons Attribution (CC BY) license (https://creativecommons.org/licenses/by/4.0/).

## 1. Introduction

In recent years, the study of dual-function radar and communication (DFRC) systems has garnered significant attention, as they offer the potential to alleviate cross-interference between radar and communication infrastructures while enhancing spectral efficiency [1–4]. To achieve the functionality of DFRC systems, integrated waveforms capable of performing both radar and communication tasks are typically designed, and matched filters (MF) are used to enhance signal quality and reduce noise interference. Nevertheless, the MF frequently exhibits elevated sidelobe levels (SLL), which can diminish the likelihood of detecting feeble targets obscured within the high sidelobes.

To address the issue of high sidelobes near the target unit, especially in scenarios with strong interference from adjacent range cells, it is necessary to suppress the near-range sidelobe interference (NRSI) they cause. The main sources of interference include environmental clutter, cross-interference from other radar systems, and adversarial electronic countermeasures. Therefore, designing a mismatched filter (MMF) to replace MF has become an effective solution [5–8].

For the design of mismatched filters aimed at sidelobe reduction and interference suppression, in [9], a complementary discrepant filter array is introduced to diminish

the sidelobe amplitude of the unequivocal output and the power of range-indeterminate reflections. In [10], it puts forward a synergistic waveform and filter methodology for coherent frequency diverse array radar, which can attenuate the sidelobes linked with range pulse compression. In [11], it introduces an innovative weighted mismatched filter (WMMF) capable of efficiently suppressing sidelobes, while preserving the requisite signal-to-noise ratio (SNR) and without altering the radar's transmission or reception components. In [12], it introduces a weighted convex optimization framework integrated with a cyclic algorithm to formulate mismatched filters that attain a versatile balance between mainlobe broadening and sidelobe attenuation. In [13–15], they all designed a specific filter that effectively suppresses the range sidelobes of the echo pulse compression for a particular transmitted waveform.

The aforementioned mismatched filter design methods aim to reduce sidelobes and suppress interference while maintaining good signal performance, such as SNR and unchanged system configuration. Each method is optimized for specific waveforms or scenarios, such as coherent frequency diverse radar or ambiguous echo energy suppression, using techniques like complementary filter groups, weighted mismatched filters, and convex optimization. However, these methods may increase the mainlobe width while suppressing sidelobes, as they do not constrain the mainlobe width, which affects range resolution. Additionally, the computational complexity of some methods is high, making them less suitable for real-time applications.

For the joint optimization design of integrated waveforms and filters, in [2], an alternating projection-maximum likelihood method is developed to achieve a more accurate calculation of the target characteristics in radar communication systems. In [16], a mismatched filter is proposed that can achieve information diffusion and sidelobe suppression using space-frequency modulation technology while reducing the SNR loss during the filtering process. In [17], a method is proposed to mitigate partial sampling repeater jamming through a joint optimization iterative algorithm. In [18], a synergistic design technique for radar waveforms and mismatched filters is proposed, aiming to suppress range sidelobes, though with an accompanying SNR degradation. In [19], a novel mismatched filtering approach is introduced, which simultaneously optimizes pulse compression and spatial beamforming. Optimizing communication performance is also essential for improving the overall system performance. In [20], it proposes a tensor-based approach to address the dual problems of channel estimation and target sensing in massive MIMO-ISAC systems. Through a shared training pattern, both channel and target parameter estimation are handled in a unified manner. In [21], the utilization of time modulated array (TMA) is proposed to enhance the age of information (AoI) in covert communication and derive a communication covertness metric based on Kullback–Leibler (KL) divergence. Compared to methods that handle these processes separately, this unified approach enhances sidelobe suppression. Meanwhile, in [22], the waveform and filter are co-designed using alternating minimization and majorization–minimization (MM) algorithms, achieving an effective reduction in radar pulse compression sidelobes while managing the associated gain attenuation. In [23–26], they all achieve sidelobe suppression and interference minimization by introducing mismatched filters, which enhance the radar system's dynamic range and detection accuracy. Moreover, they maintain low losses and consistent high performance even with changes in filter length.

The methods for joint optimization of waveforms and filters mentioned above aim to reduce radar pulse compression sidelobes, improve detection accuracy, and minimize interference. By jointly designing waveforms and mismatched filters, these methods achieve better system performance compared to separate processing while attempting to minimize signal loss. Some methods accept a certain degree of SNR loss in exchange for better

sidelobe suppression. They employ various optimization techniques, such as alternating projection, space-frequency modulation, and iterative algorithms, and are optimized for specific issues like jamming mitigation. However, common drawbacks include SNR loss and increased computational complexity.

In this letter, we utilize continuous phase modulation (CPM) signals employing nonlinear frequency modulation (NLFM) within the DFRC system. To further mitigate sidelobe interference, we propose a design methodology for the environment-based weighted mismatched filter (EWMF). Maximizing radar efficiency requires attaining an elevated signal-to-interference-and-noise ratio (SINR) and minimizing the leakage power amplification at the output of the crafted EWMF. To realize this objective, we formulate a weighted optimization problem and derive its optimal solution through the alternating direction multiplier method (ADMM). The key advantage of ADMM is its ability to deconstruct complex problems into simpler subproblems, thereby boosting solution efficiency and minimizing computational complexity. We then analyze the LPG caused by mismatched filtering and derive its lower bound using the Young inequality. Finally, we validate the algorithm's performance and the impact of communication modulation parameters through experimental simulation data. The results show that the EWMF algorithm effectively reduces NRSI.

In contrast to the WMMF introduced in [11], the innovations presented in this letter can be outlined as follows:

(1) The weighted time domain correlation matrix is introduced into the sidelobe suppression of integrated waveforms.
(2) The impact of communication modulation is considered in the EWMF design, and the mismatch filter is optimized using ADMM.
(3) For the EWMF design, we consider the impact of NRSI, while it is not considered in [11].

The subsequent sections of this letter are structured as follows: In Section 2, the DFRC waveform model is derived. Section 3 formulates and resolves the optimization problem. Section 4 presents numerical simulations. Lastly, Section 5 offers the conclusions.

The notation and corresponding representation of the symbols used in this work are summarized in Table 1.

**Table 1.** Notation and Representation.

| Notation | Representation |
|---|---|
| Non-bold letters | Scalars |
| Bold lowercase letters | Vectors |
| Bold uppercase letters/characters | Matrices |
| $[\cdot]^*$ | Conjugate |
| $[\cdot]^{\mathrm{T}}$ | Transpose |
| $[\cdot]^{\mathrm{H}}$ | Conjugate transpose |
| $\lvert\cdot\rvert$ | Absolute value of a scalar |
| $\lceil\cdot\rceil$ | Rounding up |
| $\lfloor\cdot\rfloor$ | Rounding down |
| $*$ | Convolution operator |
| $\mathrm{diag}\{\cdot\}$ | Diagonal matrix |

## 2. Design of NLFM-CPM Integrated Waveform and Signal Processing Metheds

The selection of the waveform plays a crucial role in shaping the performance of the echo signal across both range and Doppler dimensions. Conversely, the communication modulation technique influences the transmission speed and resilience of the communication data. In radar-communication integrated systems, when range resolution is not the primary concern, LFM signals are typically used as the radar baseband signal, with communication modulation applied on top. After analyzing the ambiguity functions of different radar waveforms and communication modulation methods, we ultimately selected NLFM signals as the radar baseband signal and combined them with CPM modulation to achieve communication functionality.

Compared to LFM, NLFM achieves lower range sidelobes by optimizing spectral characteristics, which helps integrate communication functionality with minimal impact on radar performance, enabling efficient resource sharing. The CPM modulation method can control the stability of communication transmission by adjusting multiple modulation parameters.

The formulation for the NLFM-CPM transmitted signal model is presented as follows:

$$s(t) = G\left(t - \frac{T_p}{2}, T_p\right) \cdot \exp[j(\varphi(t) + \phi(t; I) + \phi_0)] \tag{1}$$

$$G(t, T_p) = \begin{cases} 1, |t| \leq \frac{T_p}{2} \\ 0, |t| > \frac{T_p}{2} \end{cases} \tag{2}$$

where $G(t, T_p)$ is the envelope of the signal, $T_p$ is the signal width, $\varphi(t)$ is the phase function, and $\phi(t, I)$ denotes communication continuous phase modulation signal. $\phi(t, I)$ can be further written as

$$\phi(t, I) = \sum_{n=0}^{N_c-1} \text{rect}\big((t - nT_p)/T_p\big)\phi(t, I_n) \tag{3}$$

where $N_c$ is number of symbols, rect is the rectangular function, $\phi(t, I_n)$ is the phase value of the $n$-th symbol. $\phi(t, I_n)$ is given as

$$\phi(t, I_n) = \pi h \sum_{m=-\infty}^{n-L_c} I_m + 2\pi h \sum_{m=n-L_c+1}^{n} I_m q(t - mT_p), nT_p \leq t < (n+1)T_p \tag{4}$$

where $L_c$ is the partial response length, $I_m$ is the symbol sequence to be modulated, $I_m \in \left\{\pm 1, \pm 3, \ldots, \pm(M-1)\right\}$, $M$ is the modulation order, $h$ is the modulation index, $q(t)$ is obtained by integrating the impulse function $g(t)$.

$$q(t) = \begin{cases} 0, & t < 0 \\ \int_0^t g(\tau)d\tau, & 0 \leq t \leq L_c T_s \\ 1/2, & t > L_c T_s \end{cases} \tag{5}$$

where the raised cosine (RC) pulse $g(t)$ is

$$g(t) = \frac{1}{2L_c T_p}\left[1 - \cos\left(\frac{2\pi t}{L_c T_p}\right)\right], \quad 0 \leq t \leq L_c T_p \tag{6}$$

The RC pulse is molded using a raised cosine function, which ensures smooth transitions and minimal spectral dispersion. Additionally, the RC pulse demonstrates robust

resilience against multipath fading and interference, rendering it ideal for high-speed data transmission with a low bit error rate and high transmission efficiency. When $L_c = 1$, CPM signals are classified as full response signals. When $L_c > 1$, CPM signals are categorized as partial response signals.

The pulse repetition interval (PRI) for the transmitted signal is designated as $T$, and it must adhere to

$$T \geq 2T_p \tag{7}$$

to avoid pulse overlap and ensure accurate signal processing [27]. The total number of samples per pulse is given by

$$N = T \cdot f_s \tag{8}$$

where $f_s$ is the sampling frequency. The discrete form of $s(t)$ is

$$s(n) = s(t)\Big|_{t=\frac{n}{f_s}}, n = 0, 1, \ldots, N-1. \tag{9}$$

Consider multiple scattering points, where the target is represented by $b$ and the strong interference by $k$. The distance from the radar to the target is represented by $R_b$, and the distance from the radar to the intense interference is denoted as $R_k$. The discrete baseband echo signal $s_r(n)$ is defined as

$$s_r(n) = \sigma_t s(n - n_t) \cdot e^{-j2\pi f_c \tau_t} + \sum_{k=1}^{K} \sigma_k s(n - n_k) \cdot e^{-j2\pi f_c \tau_k} + c(n), n = 0, 1, \ldots, N-1 \tag{10}$$

where $\sigma_t$ denotes the scattering coefficient of the target point, $n_t = \lfloor \tau_t \cdot f_s \rfloor$ represents the discrete form of $\tau_t$, and $\tau_t = \frac{2R_b}{c}$ signifies the time delay of the target, with $c$ being the speed of light. Similarly, $\sigma_k$ is the scattering coefficient for the $k$-th clutter point, $n_k = \lfloor \tau_k \cdot f_s \rfloor$ is the discrete representation of $\tau_k$, and $\tau_k = \frac{2R_k}{c}$ indicates the time delay of the $k$-th clutter point. The term $c(n)$ denotes the additive noise component, and $K$ is the total number of clutter points. Thus, the discrete Fourier transform (DFT) of (10) can be computed as

$$S_r(f) = \sigma_t S(f) \exp(-j2\pi f_c \tau_t) \cdot \exp\left(-j2\pi f \frac{n_t}{N}\right) + \sum_{k=1}^{K} \sigma_k S(f) \exp(-j2\pi f_c \tau_k) \cdot \exp\left(-j2\pi f \frac{n_k}{N}\right) + C(f), \quad f = 0, 1, \ldots, N-1 \tag{11}$$

where $S(f)$ denotes the DFT of $s(n)$, $C(f)$ represents the DFT of $c(n)$. The MF $H_{\mathrm{MF}}(f)$ in the frequency domain and $S(f)$ are conjugate transpose

$$H_{\mathrm{MF}}(f) = S^*(f) \tag{12}$$

By performing an inverse discrete Fourier transform (IDFT) on the product of the input signal and the filter's frequency response, the output of MF is obtained as

$$\begin{aligned} s_{\mathrm{MF}}(n) &= \mathrm{IDFT}\{S_r(f)S^*(f)\} \\ &= \mathrm{IDFT}\left\{\sigma_t |S(f)|^2 e^{-j2\pi f_c \tau_t} e^{-j2\pi f \frac{n_t}{N}} + \sum_{k=1}^{K} \sigma_k |S(f)|^2 e^{-j2\pi f_c \tau_k} e^{-j2\pi f \frac{n_k}{N}} + W(f)S^*(f)\right\} \\ &= \sigma_t e^{-j2\pi f_c \tau_t} \cdot \mathrm{psf_w}(n - n_t) + \sum_{k=1}^{K} \sigma_k e^{-j2\pi f_c \tau_k} \cdot \mathrm{psf_w}(n - n_k) + \mathrm{IDFT}\{W(f)S^*(f)\} \end{aligned} \tag{13}$$

where $\mathrm{psf_w}(n) = \mathrm{IDFT}\{S(f)W(f)\}$ represents the calculation of the system's point spread function $\mathrm{psf}(n)$ using the signal's frequency domain power spectral density $|S(f)|^2$ [28]. In general, when the signal power is significantly higher than the noise, the influence of $\mathrm{IDFT}\{W(f)S^*(f)\}$ on the MF result can be ignored.

To illustrate the impact of near-range cells on filtering, the linear convolution [12] of all range cells $\mathbf{x}_i (i = -N+1, \cdots, N-1)$ can be represented as

$$\begin{aligned}\mathbf{\Lambda}(s) &= \begin{bmatrix}\mathbf{x}_{-N+1} & \mathbf{x}_{-N+2} & \cdots \mathbf{x}_0 & \cdots & \mathbf{x}_{N-2} & \mathbf{x}_{N-1}\end{bmatrix}^T \\ &= \begin{bmatrix} s_0 & s_1 & \cdots & s_{N-1} & 0 & \cdots & \cdots & 0 \\ 0 & s_0 & \cdots & s_{N-2} & s_{N-1} & 0 & \cdots & 0 \\ \vdots & \vdots & \ddots & \vdots & s_{N-2} & s_{N-1} & 0 & \vdots \\ \vdots & \ddots & \vdots & s_0 & \vdots & \vdots & \ddots & 0 \\ 0 & \cdots & 0 & 0 & s_0 & s_1 & \cdots & s_{N-1} \end{bmatrix}^T\end{aligned} \tag{14}$$

where $\mathbf{\Lambda}(s)$ is the linear convolution matrix constructed from the signal $\mathbf{s}$, the $P$-dimensional column vector $\mathbf{x}_0 = \left[\mathbf{0}_z^{\mathrm{T}} s_0 \cdots s_{N-1} \mathbf{0}_z^{\mathrm{T}}\right]^{\mathrm{T}}$ is formed by zero-padding both ends of the received signal, and $\mathbf{0}_z$ represents a column vector of length $z$ filled with zeros. If $\mathbf{x}_0$ represents the target information that needs to be preserved, then $\mathbf{x}_i$ $(i = -N_1+1, \cdots, -1, 1, \cdots, N_1-1)$ represents the information that is not needed. This also explains the occurrence of sidelobes in the time-domain response.

Figure 1 illustrates the arrangement of signal samples received by a radar receiver from different range cells. The target range cell and its neighboring cells are highlighted in green, showing the distribution of their received sample sequence from $S_0$ to $S_{N-1}$. These samples are utilized in the processing stage for accurate target detection. The orange area on the left represents other cells near the target range cell, while the blue area on the right represents range cells further from the target. The data from these side areas have similarities with the target cell but are temporally shifted, potentially causing sidelobe interference.

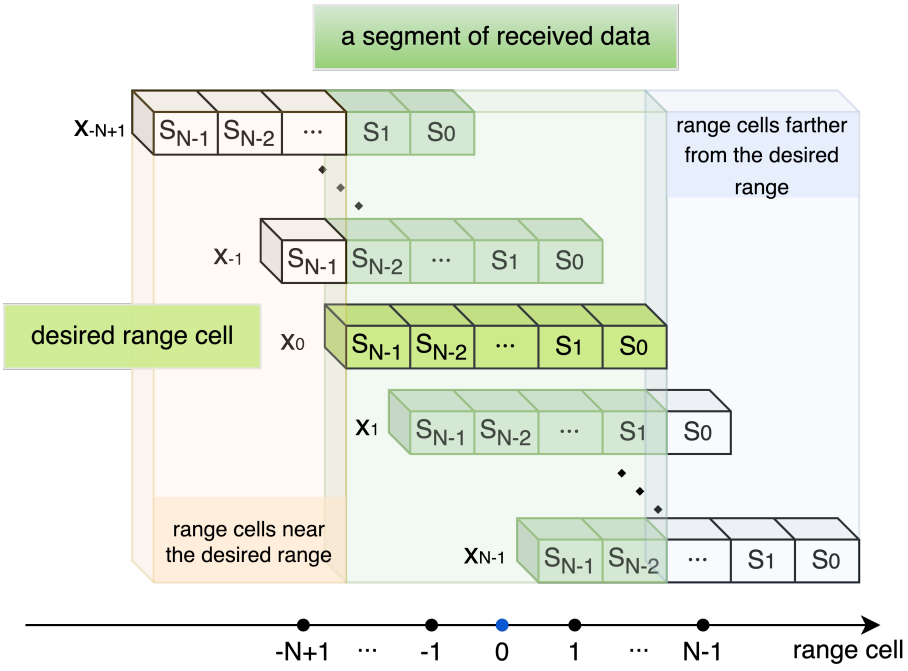



**Figure 1.** A schematic diagram of received data from different range cells.

The output of the convolution of $\mathbf{x}_i$ with $\mathbf{h}_{\mathrm{MF}} = \mathbf{x}_i^*$ can be expressed as

$$\mathbf{psf}_{\mathrm{MF}} = \mathbf{\Lambda}(s) \cdot \mathbf{h}_{\mathrm{MF}}. \tag{15}$$

The expression of the EWMF output is given by

$$\mathbf{psf}_{\mathrm{EWMF}} = \mathbf{\Lambda}(s) \cdot \mathbf{h}. \tag{16}$$

where $\mathbf{h}$ is the EWMF coefficient. (15) and (16) can also be represented in terms of range cells as

$$\mathbf{psf} = [y_{-N+1}, \cdots, y_{-1}, y_0, y_1, \cdots, y_{N-1}]^{\mathrm{T}} \tag{17}$$

where $y_0$ represents the main peak value of the mainlobe, and the values in the sidelobe region corresponds to $y_i (i = -N+1, \ldots, -1, 1, \ldots, N-1)$.

## 3. Joint Design Algorithm of NLFM-CPM Waveform and Environment-Based Weighted Mismatched Filter (EWMF)

### *3.1. Weighted Time Domain Correlation Matrix Design*

Refining the design of the matched filter to attenuate sidelobe intensity constitutes a pivotal element in augmenting system efficacy. The mainlobe indicates the target's position, while sidelobes typically increase the detection threshold around the target and obscure weak signals. Therefore, it is necessary to suppress high sidelobes near the target. The diagonal matrix composed of weighted coefficients in the time domain is defined as

$$\mathbf{w} = \mathrm{diag}[w(-N+1), \cdots, w(-1),\ w(0),\ w(1), \cdots, w(N-1)] \tag{18}$$

where $w(i)$ is the weighting coefficients of manual intervention in the updating Formula (36), $i \in \mathbb{Z} \cap [-N+1, N-1]$ corresponds to the weighted coefficients of the desired mainlobe and other sidelobe regions. We defined the $2N-1$-point IDFT matrix as

$$\mathbf{F}_{2N-1}^{-1} = \frac{1}{2N-1} \begin{bmatrix} 1 & 1 & \cdots & 1 \\ 1 & W_{2N-1}^{-1} & \cdots & W_{2N-1}^{-(2N-2)} \\ \vdots & \vdots & \ddots & \vdots \\ 1 & W_{2N-1}^{-(2N-2)} & \cdots & W_{2N-1}^{-(2N-2)(2N-2)} \end{bmatrix} \tag{19}$$

where $W_{2N-1}^{-k} = \exp\left(j\frac{2\pi}{2N-1}k\right)$. Thus, (15) can be rewritten as

$$\mathbf{psf}_{\mathrm{MF}} = \mathbf{F}^{-1}\mathbf{S}_{\mathrm{P}} \tag{20}$$

and

$$\mathbf{S}_{\mathrm{P}} = \mathbf{S} \odot \mathbf{S}^{*} \tag{21}$$

Without considering the loss of process gain (LPG) of the EWMF, the $\mathbf{psf}_{\mathrm{EWMF}}$ is defined as [11]

$$\mathbf{psf}_{\mathrm{EWMF}} = \mathbf{F}^{-1}(\mathbf{S}_{\mathrm{P}} \odot \mathbf{W}) \tag{22}$$

where $\odot$ is the Hadamard product, $\mathbf{W}$ is the DFT of $\mathbf{w}$.

Some early literature often employed the minimization of the ISL criterion to reduce sidelobes. The ISL of the EWMF output is

$$\mathbf{Y}_{\mathrm{ISL}} = \mathbf{h}^{*}(\mathbf{\Lambda}(\mathbf{s})\mathbf{w}_{\mathrm{ini}}\mathbf{\Lambda}^{*}(\mathrm{s}))\mathbf{h} = \mathbf{F}^{-1}(\mathbf{S}_{\mathrm{P}} \odot \mathbf{W}_{\mathrm{ini}}) \odot \mathbf{F}^{-1}(\mathbf{S}_{\mathrm{P}} \odot \mathbf{W}_{\mathrm{ini}})^{*} \tag{23}$$

where $\mathbf{w}_{\mathrm{ini}} = \mathrm{diag}(1 \cdots 1\ 0\ 1 \cdots 1)$ is just a linear weighting of the sidelobes.

However, the distribution of targets in range is typically non-uniform. In order to reduce the sidelobe gain for detecting the desired range cell, it is necessary to iteratively optimize the filter coefficients.

The weighted time domain correlation matrix (WTDCM) for the sidelobe region, based on the weighted matrix $\mathbf{w}$, is represented as

$$\mathbf{B} = \mathbf{\Lambda}(\mathbf{s})\mathbf{w}\mathbf{\Lambda}^*(\mathbf{s}) = \sum_{i=-N+1}^{N-1} w(i)\mathbf{x}_i\mathbf{x}_i^* \tag{24}$$

For the initialization of $w(i)$, we set the initial value of the manual intervention power in the sidelobe region to 1 and the initial value in the mainlobe region to 0. According to (24) and (25), the ISL output result of the EWMF can be expressed as

$$\mathbf{Y}_{\text{ISL}} = \mathbf{h}^*\mathbf{B}\mathbf{h} \tag{25}$$

*3.2. EWMF Design Based on the ADMM Algorithm*

Based on the minimum ISL criterion and subject to constraints on the mainlobe gain, it is framed as

$$\begin{aligned} &\min_{\mathbf{h}} \ \mathbf{h}^*\mathbf{B}\mathbf{h} \\ &\text{s.t} \quad \mathbf{x}_0^*\mathbf{h} = 1 \end{aligned} \tag{26}$$

In (26), the constrained mainlobe includes only one point. If the constrained mainlobe range is larger, the linear constraints can be extended to multiple range cells. Assuming the constraint on the mainlobe spans $L$ range cells near the main peak, covering $k_l$ range cells to the left and $k_r$ range cells to the right, the constrained mainlobe range can be represented as

$$\begin{aligned} &\mathbf{C} = \text{span}(\mathbf{x}_i), i \in \mathfrak{G} \\ &\mathfrak{G} = [-k_l, -(k_l-1), \cdots -1, 0, 1, \cdots, k_r] \\ &\quad k_r - k_l + 1 = L. \end{aligned} \tag{27}$$

where $i \in \mathfrak{G}$ is the mainlobe constraint matrix. (26) can be extended to the following optimization problem

$$\begin{aligned} &\min_{\mathbf{h}} \ \mathbf{h}^*\mathbf{B}\mathbf{h} \\ &\text{s.t} \quad \mathbf{C}^*\mathbf{h} = \mathbf{g} \end{aligned} \tag{28}$$

where $\mathbf{g}$ is a constant vector of length $L \times 1$ corresponding to the gain constraint.

To regulate the LPG, the design problem incorporates constraints on waveform energy, filter energy, and pulse compression peak level. The filter's energy is controlled through a direct constraint [29], while the waveform is bound by a constant modulus ensuring total energy equals $N$ [30,31]. The peak constraint, $\mathbf{h}^{\text{H}}\mathbf{x}$, depends on both the waveform and the filter. The objective function minimizes the squared deviation between the peak and a predefined threshold, $|\mathbf{h}^{\text{H}}\mathbf{x} - b_{\max}|^2$, where $b_{\max}$ is the target peak level. (28) is rewritten as

$$\begin{aligned} &\min_{\mathbf{h}} \left\| \mathbf{B}^{1/2}\mathbf{h} \right\|_2^2 + \mu|\mathbf{h}^H\mathbf{x} - b_{\max}|^2 \\ &\text{s.t } \mathbf{C}^*\mathbf{h} = \mathbf{g} \\ &\quad \mathbf{x}^H\mathbf{h} = \mathbf{x}^H\mathbf{x} \\ &\quad \mathbf{x}^H\mathbf{E}_n\mathbf{x} \le \eta, n = 1, 2, \ldots, N \end{aligned} \tag{29}$$

where the constraint $\mathbf{x}^H\mathbf{h} = \mathbf{x}^H\mathbf{x}$ is mainly included to discard the null solution, $\mathbf{g}$ is a constant vector of length $L$ corresponding to the gain constraint, $b_{\max}$ is the predefined peak level, $\mu$ denotes the weight between the two objective functions, and the matrixes $\mathbf{E}_n$ is defined by

$$\mathbf{E}_n(i,j) = \begin{cases} 1 & i = j = n \\ 0 & else. \end{cases} \tag{30}$$

To transform the given optimization problem into a second order cone problem (SOCP), we need to appropriately reformulate the objective function and constraints. First, expand the absolute value term by introducing two new variables, $\mathbf{v} = \mathbf{B}^{1/2}\mathbf{h}$ and $t = |\mathbf{v}^{\mathrm{H}}\mathbf{B}^{-1/2}\mathbf{x} - b_{\max}|$. The objective function is rewritten as

$$\begin{aligned} &\min_{\mathbf{v},t,\mathbf{u}} \|\mathbf{v}\|_2^2 + \mu t^2 \\ &\text{s.t } \mathbf{C}^*\mathbf{B}^{-1/2}\mathbf{v} = \mathbf{g} \\ &\quad \mathbf{x}^H\mathbf{B}^{-1/2}\mathbf{v} = \mathbf{x}^H\mathbf{x} \\ &\quad t \geq \|\mathbf{u}\|_2 \\ &\quad \mathbf{u}^H\mathbf{u} \leq z \\ &\quad z \leq |\mathbf{v}^H\mathbf{B}^{-1/2}\mathbf{x} - b_{\max}|^2 \\ &\quad \mathbf{x}^H\mathbf{E}_n\mathbf{x} \leq \eta, n = 1,2,\ldots,N \end{aligned} \tag{31}$$

The ADMM method is ideal for this problem as it simplifies complex optimization tasks by breaking them into manageable subproblems and managing various constraints, including second-order cone and nonlinear equality constraints, by incorporating them into the augmented Lagrangian function. It is expressed as

$$\begin{aligned} L(\mathbf{v},t,\mathbf{u},\boldsymbol{\lambda},\gamma,\mu_1,\mu_2,\boldsymbol{\nu},\rho,\mu) &= \|\mathbf{v}\|_2^2 + \mu t^2 \\ &+ \frac{\rho}{2}\|\mathbf{C}^*\mathbf{B}^{-1/2}\mathbf{v} - \mathbf{g} + \boldsymbol{\lambda}\|_2^2 - \frac{\rho}{2}\|\boldsymbol{\lambda}\|_2^2 \\ &+ \frac{\rho}{2}\left(|\mathbf{x}^H\mathbf{B}^{-1/2}\mathbf{v} - \mathbf{x}^H\mathbf{x} + \gamma|^2 - |\gamma|^2\right) \\ &+ \frac{\rho}{2}\left((t - \|\mathbf{u}\|_2 + \mu_1)^2 - \mu_1^2\right) \\ &+ \frac{\rho}{2}\left(\left|\mathbf{u}^H\mathbf{u} - |\mathbf{v}^H\mathbf{B}^{-1/2}\mathbf{x} - b_{\max}|^2 + \mu_2\right|^2 - |\mu_2|^2\right) \\ &+ \sum_{n=1}^{N}\frac{\rho}{2}\left((\mathbf{x}^H\mathbf{E}_n\mathbf{x} - \eta + \nu_n)^2 - \nu_n^2\right) \end{aligned} \tag{32}$$

where $\rho$ is called the penalty parameter. To write the update iterations for this problem in the style of ADMM, we need to update $\mathbf{v}$, $t$, $\mathbf{u}$, $\boldsymbol{\lambda}$, $\gamma$, $\boldsymbol{\mu}$, and $\boldsymbol{\nu}$ iteratively. Here is a general outline of the update steps:

$$\begin{cases} \mathbf{v}^{k+1} = \arg\min_{\mathbf{v}} L(\mathbf{v}, t^k, \mathbf{u}^k, \boldsymbol{\lambda}^k, \gamma^k, \mu_1^k, \mu_2^k, \boldsymbol{\nu}^k, \rho, \mu) \\ t^{k+1} = \arg\min_{t}\left\|\mathbf{v}^{k+1} - t^k + \mu_1^k\right\|^2 \\ \mathbf{u}^{k+1} = \mathbf{v}^{t+1} + \mu_2^k \\ \boldsymbol{\lambda}^{k+1} = \mathbf{v}^{k+1} - \mathbf{g} + \boldsymbol{\lambda}^k \\ \gamma^{k+1} = \mathbf{x}^H\mathbf{B}^{-1/2}\mathbf{v}^{k+1} - \mathbf{x}^H\mathbf{x} + \gamma^k \\ \mu_1^{k+1} = t^{k+1} - \|\mathbf{u}\|_2 + \mu_1^k \\ \mu_2^{k+1} = \mathbf{u}_{k+1}^H\mathbf{u}_{k+1} - \left|\mathbf{v}^{k+1}\mathbf{B}^{-1/2}\mathbf{x} - b_{\max}\right|^2 + \mu_2^k \\ \boldsymbol{\nu}_n^{k+1} = \mathbf{x}^H\mathbf{E}_n\mathbf{x} - \eta + \boldsymbol{\nu}_n^k, \quad n = 1,2,\ldots,N \end{cases} \tag{33}$$

where $k$ represents the iteration index. First, the update for $\mathbf{v}$ is addressed. By optimizing $\mathbf{v}$ while keeping the auxiliary and dual variables constant, its minimization is derived

through partial derivatives. Next, with $\mathbf{v}$, $t$, and other variables held constant, the auxiliary variable $\mathbf{u}$ is updated using the latest values. The analytical solution for $\mathbf{x}$ is given by

$$\mathbf{x}^{k+1} = \mathbf{B}^{1/2}\left(\frac{b_{\max} \pm \sqrt{\mathbf{u}_{k+1}^H \mathbf{u}_{k+1} - \Delta\mu_2}}{\mathbf{v}^{k+1}}\right). \tag{34}$$

Thirdly, $\mathbf{h}$ is updated for the fixed $\mathbf{x}$, $\mathbf{v}$, and other variables fixed. The analytical solution of $\mathbf{h}$ is expressed as:

$$\mathbf{h}^{k+1} = \frac{\mathbf{v}^{k+1} + \rho(\mathbf{B}^{-1/2}\mathbf{C}\mathbf{g} + \mathbf{B}^{-1/2}\mathbf{x}_{k+1}\mathbf{x}_{k+1}^H\mathbf{x}_{k+1})}{\mathbf{B}\left(\mathbf{I} + \rho(\mathbf{B}^{-1/2}\mathbf{C}\mathbf{C}^*\mathbf{B}^{-1/2} + \mathbf{B}^{-1/2}\mathbf{x}_{k+1}\mathbf{x}_{k+1}^H\mathbf{B}^{-1/2})\right)} \tag{35}$$

Based on prior knowledge of the environmental range, the desired reference template sidelobe shape is predefined. The desired reference template sidelobe shape is denoted by $D(i)$, where $i$ represents the $i$-th range cell. We further define the filter weight based on the environmental reference template as $w(i)$. When $i \in \mathfrak{G}$, $w(i) = 0$. When $i \notin \mathfrak{G}$, $w(i)$ can be expressed as follows:

$$w^{k+1}(i) = w^k(i) + \frac{\lambda w^k(i)\left[|y_k(i)| - \Pr^k D(i)\right]}{\Pr^k D(i)} + \beta \cdot (w^k(i) - w^{k-1}(i)) \tag{36}$$

where $\lambda$ is an iteration coefficient, $\Pr^k \mathrm{D}(i)$ is the extent to which the reference template is linearly scaled to the minimum peak level, known as the absolute level [32], and $\beta$ is a momentum coefficient used to smooth the iteration process and prevent getting stuck in local optima. Compare the level of a certain range cell with the levels of its adjacent cells on both sides. If its level is higher than that of the adjacent cells, it is considered a peak level. The smallest of all the peak levels is identified as the lowest peak level $\Pr^k$. The algorithm steps for the joint design of NLFM-CPM waveform and EWMF based on ADMM are shown in Table 2.

**Table 2.** The algorithm steps for the joint design of NLFM-CPM waveform and EWMF based on ADMM.

| Input | $\mathbf{w}_{\text{ini}}$, $\mathbf{\Lambda}(\mathbf{s})$, $\mathbf{C}$, $\mathbf{g}$, $b_{\max}$, $k = 0$, $K$, and auxiliary variables. |
|---|---|
| Output | EWMF coefficients: $\mathbf{h}$, $\mathbf{x}$. |
| Processing Steps | |
| Step 1 | Set $k = k + 1$. Compute $\mathbf{B}$ using Equation (24) and $\mathbf{y}_{\text{ISL}}$ using Equation (25). |
| Step 2 | Compute $\mathbf{u}$, $\mathbf{x}$, and $\mathbf{h}$ by minimizing the metric using Equations (33), (34) and (35), respectively. Update other variables using Equation (33). |
| Step 3 | Identify the lowest peak level $\Pr^k$ as the reference level. Form a new reference template based on $\Pr^k$ and compute $w(i)$ using Equation (36). |
| Step 4 | Repeat Step 1 until $k = K$ or $\left\|w^{k+1}(i) - w^k(i)\right\| < \epsilon$, where $\epsilon \to 0$. |

### *3.3. LPG Analysis*

LPG is characterized as the ratio between the SNR enhancement obtained via EWMF and that of the MF. The expression for this relationship is outlined below.

$$\mathrm{LPG} = 10\log_{10}\left(\frac{\mathrm{SNR}_{\mathrm{MF}}}{\mathrm{SNR}_{\mathrm{EWMF}}}\right) \tag{37}$$

The total noise power $P_n$ and the maximal signal power output $P_s$ of the EWMF output are respectively

$$P_n = \frac{N_0}{4\pi} \sum_{n=-N+1}^{N-1} w^2(n) * |x(n)|^2 \tag{38}$$

$$P_s = \frac{1}{4\pi^2} \left| \sum_{n=-N+1}^{N-1} w(n) * |x(n)|^2 \right|^2. \tag{39}$$

where $*$ represents the convolution operation; $\frac{N_0}{2}$ is the power spectral density of the white noise. We can get the output SNR of the EWMF as

$$\mathrm{SNR}_{\mathrm{EWMF}} = \frac{P_s}{P_n} = \frac{1}{\pi N_0} \cdot \frac{\left| \sum_{n=-N+1}^{N-1} w(n) * |x(n)|^2 \right|^2}{\sum_{n=-N+1}^{N-1} w^2(n) * |x(n)|^2} \tag{40}$$

The output SNR of the MF can be easily derived from Equation (40) by setting $W(k) \equiv 1$

$$\mathrm{SNR}_{\mathrm{MF}} = \mathrm{SNR}_{\mathrm{EWMF}}\Big|_{w(n)\equiv 1} = \frac{1}{\pi N_0} \cdot \frac{\left| \sum_{k=-N+1}^{N-1} |x(n)|^2 \right|^2}{\sum_{k=-N+1}^{N-1} |x(n)|^2} = \frac{1}{\pi N_0} \sum_{n=-N+1}^{N-1} |x(n)|^2 \tag{41}$$

For a given $N_0$, the $\mathrm{SNR}_{\mathrm{MF}}$ is determined exclusively by the power of the waveform itself, in accordance with the principles of the matched filter. Subsequently, the SNR loss is defined as the ratio of $\mathrm{SNR}_{\mathrm{MF}}$ to $\mathrm{SNR}_{\mathrm{EWMF}}$.

$$\mathrm{LPG} = 10 \log_{10} \left( \frac{\mathrm{SNR}_{\mathrm{MF}}}{\mathrm{SNR}_{\mathrm{EWMF}}} \right) = 10 \log_{10} \left( \frac{\sum_{n=-N+1}^{N-1} |x(n)|^2 \cdot \sum_{n=-N+1}^{N-1} w^2(n) * |x(n)|^2}{\left| \sum_{n=-N+1}^{N-1} w(n) * |x(n)|^2 \right|^2} \right) \tag{42}$$

Young's inequality states that for two signals $f(n)$ and $g(n)$ [33], we have

$$\|f * g\|_r \leq \|f\|_p \cdot \|g\|_q \tag{43}$$

where $\frac{1}{r} = \frac{1}{p} + \frac{1}{q} - 1$. Let $r = q = p = 1$, $f(n) = w(n) * |x(n)|$, and $g(n) = |x(n)|$. Substituting these into (43), we obtain

$$\begin{aligned} \left| \sum_{n=-N+1}^{N-1} w(n) * |x(n)|^2 \right|^2 &= \left| \sum_{n=-N+1}^{N-1} w(n) * |x(n)| * |x(n)| \right|^2 \\ &\leq \sum_{n=-N+1}^{N-1} \left| w^2(n) * |x(n)|^2 \right| \cdot \sum_{n=-N+1}^{N-1} |x(n)|^2. \end{aligned} \tag{44}$$

Therefore, according to Young's inequality, we can conclude that

$$\begin{aligned} \mathrm{SNR}_{\mathrm{MF}} &\geq \mathrm{SNR}_{\mathrm{EWMF}} \\ \mathrm{LPG} &\geq 0. \end{aligned} \tag{45}$$

The only factor affecting SNR loss is $w(i)$, which is determined by the reference template $D(i)$. Since there is no simple linear relationship between $\mathrm{SNR}_{\mathrm{loss}}$ and $w(i)$, it is not possible to directly determine the SNR loss caused by changes in $D(i)$ using (42). However, the SNR loss corresponding to all possible $D(i)$ values under the same parameters

can be provided as the main sidelobe level over a specified region (MSLSR) changes [11]. Based on the reference templete $D(i)$ in (36), the MSLSR is given as

$$\text{MSLSR} = 20 \cdot \log_{10}\left[\frac{1}{|\text{psf}(0)|} \cdot \frac{\sum_{i=R_x}^{R_y} |D(i) \cdot \text{psf}(k)|}{R_y - R_x + 1}\right] \tag{46}$$

where $\frac{1}{|\text{psf}\,(0)|}$ is used as a normalized coefficient, $i \in [R_x, R_y]$ denotes the region of the suppressed sidelobes.

### *3.4. Complexity*

The computational complexity of the proposed method stems from (35). The operation described in (35) incurs a computational complexity of $O(N^3)$. Given that the waveform and filter are optimized in an alternating fashion, the overall computational complexity of the proposed algorithm is $O(KN^3)$.

## 4. Numerical Simulations

In this chapter, we validate the effectiveness of the EWMF algorithm through simulation experiments that assess the impact of communication parameters and radar detection performance on the system. We set the pulse duration and bandwidth of the transmitted signal to 20 μs and 10 MHz in the monostatic system, respectively. The initial waveform uses an NLFM-CPM waveform with binary modulation and an LRC pulse envelope. The maximum number of iterations is 50, with a stopping threshold $\delta = 1 \times 10^{-4}$. The initial SINR is $-45$ dB. The main lobe of strong clutter is at the 65th range cell, and a weak target at the 55th range cell is buried by the strong clutter sidelobe.

In Figure 2a, the symbol error rate (SER) of different pulse envelopes (Lorentzian pulse, Rectangular pulse, GMSK pulse, Raised Cosine pulse) is compared across various signal-to-noise ratio (SNR) levels. The "Bound $M = 2$, $h = 0.5$" line represents the theoretical lower bound for SER performance, given a 2-phase modulation and a modulation index of 0.5. From the curves in the figure, we can observe that the Raised Cosine pulse has the closest SER performance to the theoretical lower bound, exhibiting the best error rate performance. This is because the Raised Cosine envelope provides good spectral efficiency and noise resistance, which effectively lowers the error rate at a given SNR. Additionally, the smooth shape of the Raised Cosine envelope helps suppress sidelobes in the frequency domain, reducing spectral leakage, which is crucial for minimizing error rates.

In contrast, the Rectangular pulse performs poorly at lower SNR levels. The Rectangular pulse has higher sidelobes in the frequency domain, leading to significant spectral leakage and inter-symbol interference, which introduces more errors at low SNR, resulting in a higher SER. In summary, the Raised Cosine pulse achieves the best error rate performance due to its smooth spectrum characteristics, while the Rectangular pulse has worse error rates due to its higher spectral sidelobes. This explains the performance differences in SER among the different pulse envelopes shown in the figure.

Figure 3 shows the amplitude response characteristics of four different reference template sidelobe shapes, each with unique features suited for specific applications. The linear envelope remains stable across the filter length without significant amplitude changes, making it ideal for applications that require a uniform sidelobe level in the spectrum. It has a simple design and minimizes ripple effects, though it may be less effective in scenarios requiring precise sidelobe suppression. The concave envelope drops sharply in the middle and quickly recovers on both sides, making it suitable for applications that need strong suppression at the center frequency while allowing higher sidelobes at other frequencies; the sharp dip helps isolate or attenuate unwanted frequencies at the

filter's center. The arc-shaped envelope shows a gradual, smooth decline, forming an arc curve and balancing sidelobe suppression with a smooth transition, making it suitable for applications requiring smoother transitions. It serves as a compromise between the linear and concave designs. The V-shaped envelope remains stable at both ends and drops sharply in the middle, creating a distinct V shape, which is useful for applications needing strong suppression at the center frequency and stability at the edge frequencies. It is similar to the concave envelope but with sharper transitions, helping to focus suppression in a narrow frequency band while maintaining stability at the edges. In summary, the linear envelope is for uniformity, the concave envelope for center frequency suppression, the arc-shaped envelope for smooth transitions, and the V-shaped envelope for focused center suppression and edge stability.

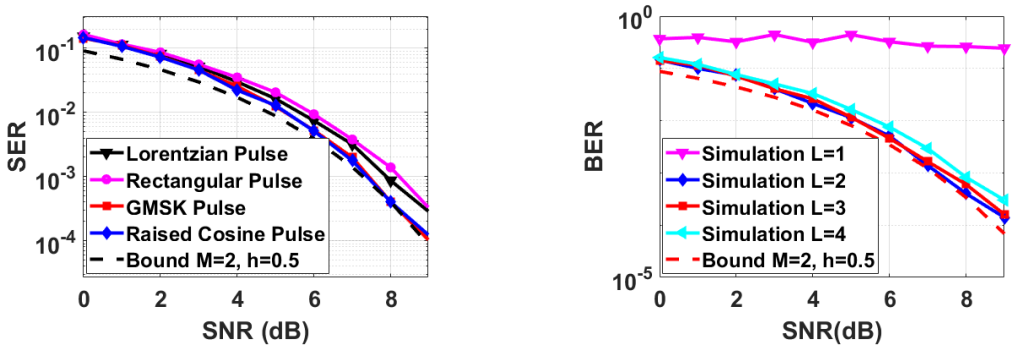



**Figure 2.** (**a**): With $M = 2$ and $h = 0.5$, the correlation between SNR and BER across various frequency pulse formulations. (**b**): With $M = 2$ and $h = 0.5$, the correlation between SNR and BER for differing partial response lengths.

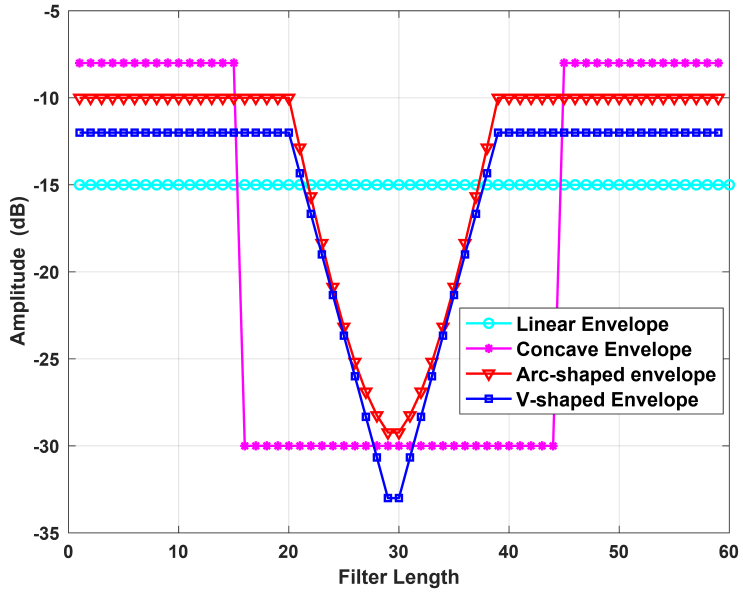



**Figure 3.** The different reference template sidelobe shapes.

In Figure 4, we compared the five highest peaks obtained after pulse compression processing, and the results indicate varying levels of signal loss caused by different template envelopes. The observed phenomenon arises from the different strategies used by traditional sidelobe suppression methods and the V-shaped filter in handling sidelobes. Traditional methods typically reduce sidelobes by smoothing the signal envelope, but they often have limited effectiveness in suppressing the first sidelobe, especially in the presence

of strong clutter. Strong clutter can cause the first sidelobe to be prominent, making it difficult for conventional methods to effectively suppress it.

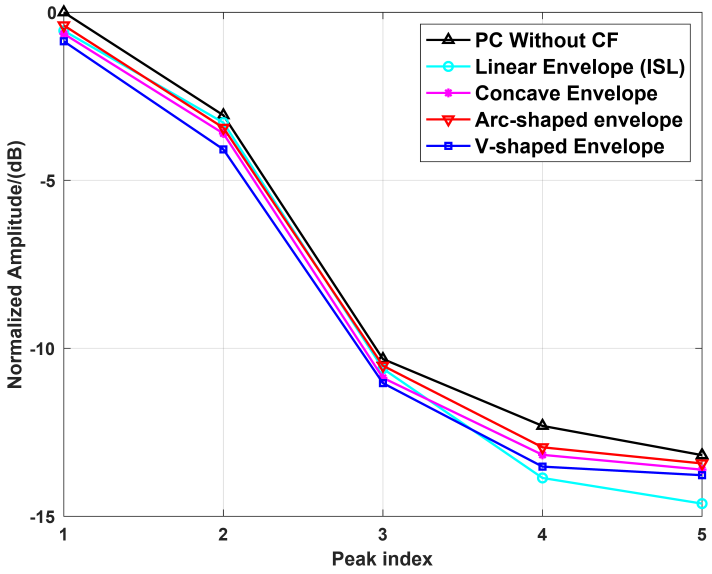



**Figure 4.** Different filter envelopes for the normalized peak loss obtained by the EWMF method.

In contrast, the V-shaped filter focuses on reducing sidelobes near strong clutter. By optimizing the frequency response for specific frequency bands, it significantly reduces the sidelobes close to strong clutter. However, this comes at the cost of increasing distant sidelobes, which can lead to more interference in other regions. While the V-shaped filter effectively detects weak targets near strong clutter, its unbalanced sidelobe suppression inevitably results in a loss of pulse compression gain, reflected in the 0.86 dB decrease in compression gain.

Figure 5a–c shows the results of employing the initial algorithm with an explicit solution, based on the Barker code, P3 code, and P4 code, respectively. As the main sidelobe level over a specified region (MSLSR) decreases, the SNR loss increases. The outcomes of the iterative algorithm, grounded in the LFM, NLFM, and NLFM-CPM waveforms, are illustrated in Figure 5d–f, respectively. Owing to minor variations in the iterative depth, the curves exhibited in (d)–(f) are less smooth relative to those of the phase code, but the overall trends persist unchanged. We selected all sidelobes outside the 3 dB mainlobe width as the range for calculating the MSLSR, with $R_x = 60$ and $R_y = 70$. The minimum MSLSR is established at $-80$ dB, and the MSLSR attainable for mitigating all sidelobes using the NLFM-CPM waveform is approximately $-80$ dB.

The observed phenomenon results from the balance between sidelobe suppression and SNR loss across different waveform structures and algorithm optimization strategies. Phase-coded waveforms like Barker, P3, and P4 exhibit strong sidelobe suppression but lead to higher SNR losses, whereas frequency-modulated waveforms such as LFM, NLFM, and NLFM-CPM demonstrate greater sidelobe suppression under iterative algorithms, albeit with slightly reduced curve smoothness. Ultimately, the NLFM-CPM waveform achieves sidelobe suppression down to $-80$ dB outside the 3 dB mainlobe width while maintaining relatively low SNR loss.

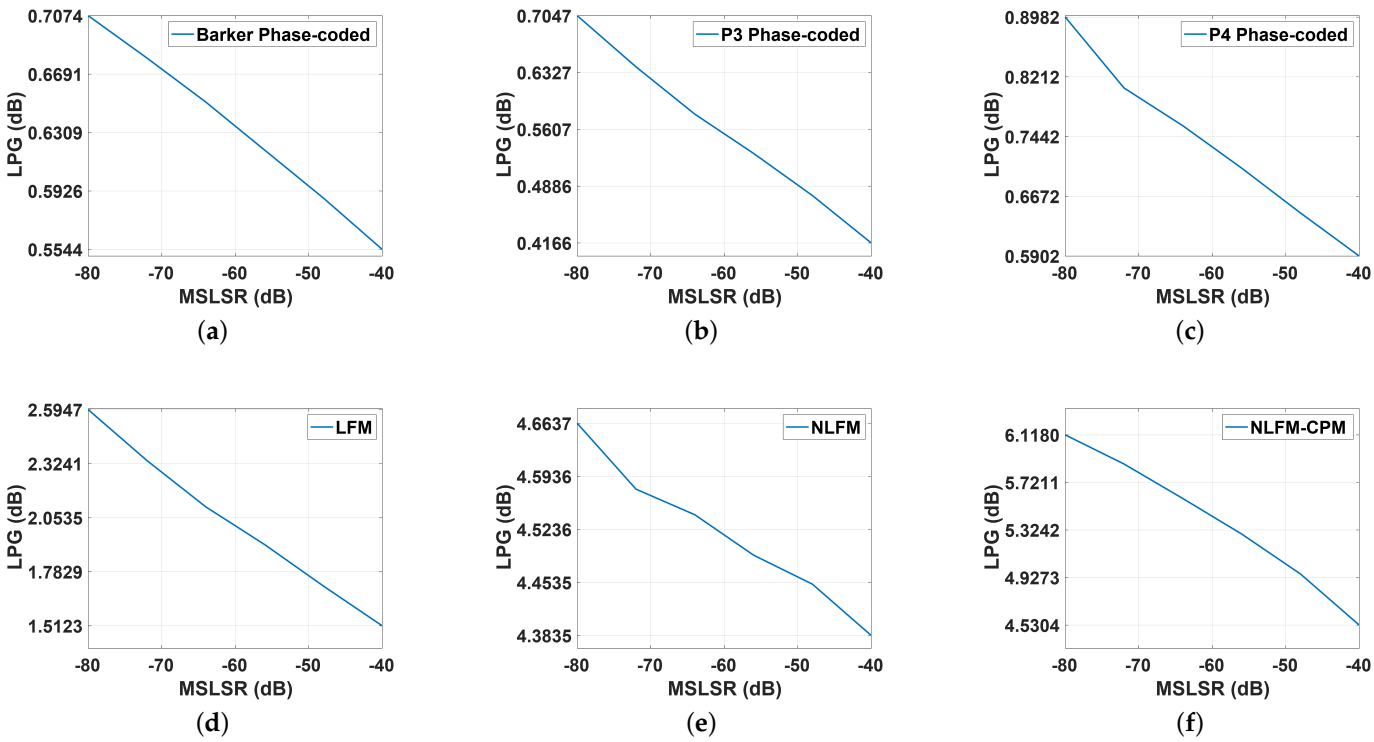



**Figure 5.** LPG for attenuating all range sidelobes derived from the following baseband signals: (**a**) Barker code, (**b**) P3 code, (**c**) P4 code, (**d**) LFM, (**e**) NLFM, and (**f**) NLFM-CPM waveform.

Figure 6 shows the normalized amplitude of the first sidelobe's peak and trough values as a function of the cavity depth of the reference template. The red curve represents the normalized peak value of the first sidelobe, which remains relatively stable around −40 dB across different cavity depths until it increases sharply near 70 dB. This stability suggests that the peak of the first sidelobe is not significantly affected by the cavity depth in the lower range but begins to rise as the depth approaches 70 dB, indicating a weakening in sidelobe suppression effectiveness at this depth. The blue curve represents the normalized trough value of the mainlobe, which initially decreases as the cavity depth increases, reaching its lowest point around 40 dB, and then gradually rises as the cavity depth continues to increase. This trend indicates that the trough value is more sensitive to changes in cavity depth, with the minimum value suggesting optimal sidelobe suppression effectiveness.

The difference between the two curves—specifically the gap between the peak and trough values—indicates the effectiveness of suppression. The maximum separation between the red and blue curves occurs around 35 dB to 40 dB. In this range, the amplitude of the first sidelobe trough is minimized relative to its peak, achieving optimal suppression. Beyond this range, as the cavity depth increases, the difference between the two curves decreases, implying a reduction in suppression effectiveness. Thus, an optimal cavity depth for the reference template lies within 35 dB to 40 dB, where the balance between minimizing the trough and maintaining a stable peak provides effective sidelobe suppression.

Figure 7 shows the impact of code lengths P = 30, P = 40, and P = 50 on the peak clutter sidelobe as SINR varies. The longer the code length or the higher the input SINR, the more likely the mainlobe of the target exceeds the level of the PSL of strong interference. Conversely, under the same PSL, a longer code length requires a lower input SINR. This implies that under identical experimental conditions, a longer code length is more adept at detecting weak targets near strong clutter in the presence of a reference template.

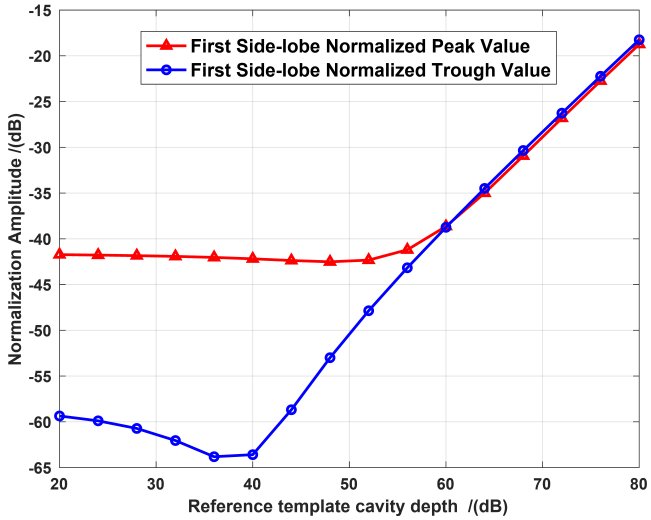



**Figure 6.** Curve of strong interference first sidelobe peak and trough values as a function of reference template cavity depth.

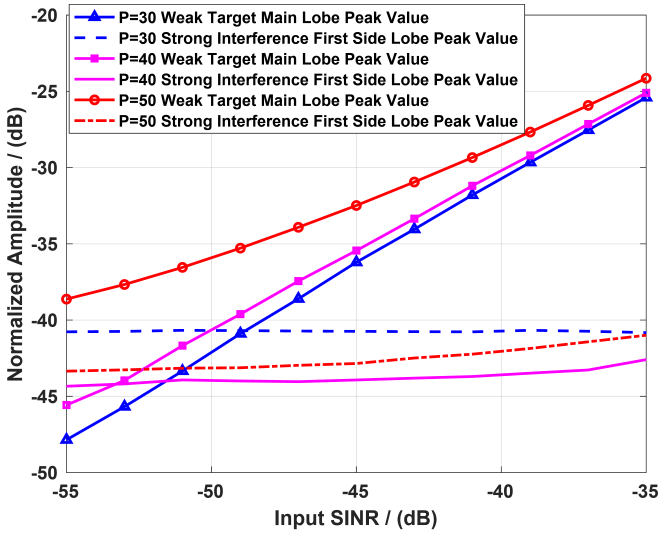



**Figure 7.** With different lengths of codes, the PSL after mismatch filtering varies with the change in input SINR.

In CPM modulation, the Modulation Index $h$ determines the magnitude of phase variation with each symbol, directly affecting the spectral efficiency and characteristics of the modulation waveform. A smaller $h$ results in smoother phase transitions, improving bandwidth efficiency, while a larger $h$ enhances signal distinguishability and improves noise resistance. Therefore, selecting an appropriate $h$ is crucial for balancing bandwidth usage and bit error rate performance. Additionally, the value of $h$ also directly impacts the size of LPG.

Figure 8 indicates that an increase in the modulation index $h$ generally leads to higher LPG. However, the curve shows fluctuations at certain points, reflecting a complex nonlinear relationship. This suggests that while the Modulation Index significantly impacts LPG, the relationship is not a simple linear decrease. This is because a larger $h$ value leads to faster phase changes, which effectively suppress the sidelobe level of the signal, thereby reducing LPG.

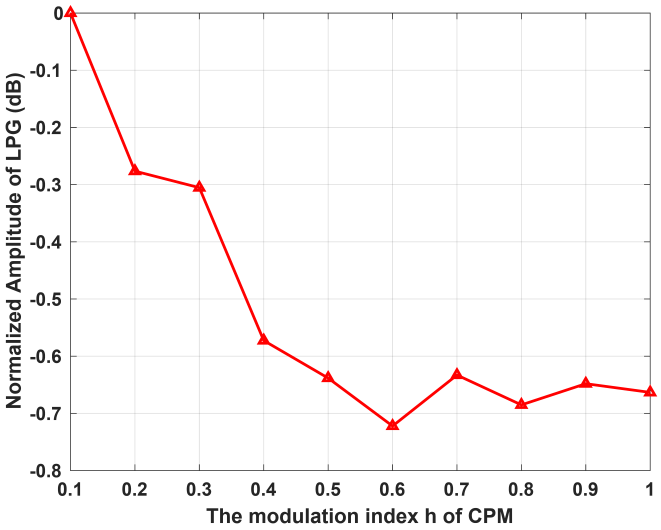



**Figure 8.** The relationship between the Modulation Index *h* of CPM and the LPG after mismatch filtering.

In Figure 9, it illustrates the variation of the objective function (ISL) during the iterative optimization process for different waveforms: P3 code, LFM, and NLFM-CPM. It can be observed that the ISL values for all three waveforms significantly decrease as the number of iterations increases, indicating that the iterative optimization process effectively reduces the ISL. Among them, the NLFM-CPM curve decreases the fastest, demonstrating the quickest convergence rate. Its final ISL value is also the lowest, showcasing its superior sidelobe suppression performance. In contrast, LFM is second-best, while the P3 code has the highest final ISL value, indicating relatively poorer performance.

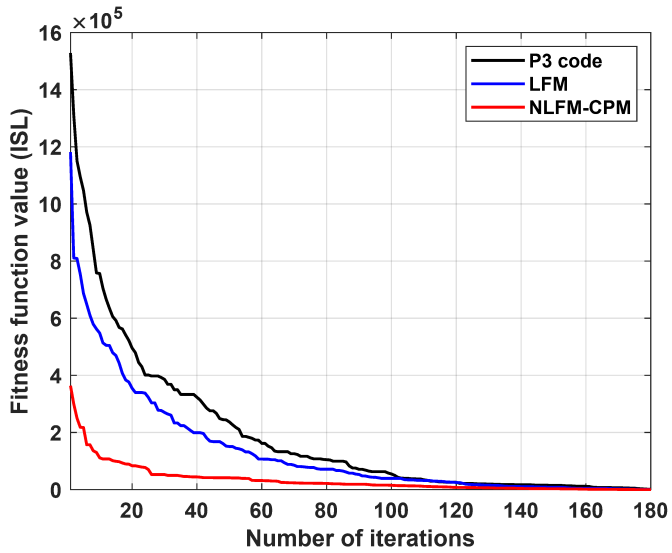



**Figure 9.** The ISL fitness function values obtained after iterating with the ADMM algorithm for different waveforms.

At the initial state, the P3 code exhibits the highest ISL value, while NLFM-CPM has the lowest, suggesting that NLFM-CPM inherently possesses better characteristics. Moreover, during the first 20 iterations, the ISL values for NLFM-CPM and LFM decrease rapidly, whereas the P3 code shows a slower decline. After approximately 50 iterations, the reduction rates for all three waveforms gradually level off. This demonstrates that the NLFM-CPM waveform has significant advantages in sidelobe suppression and convergence

speed during optimization, outperforming both LFM and P3 code. The LFM performs moderately, while the P3 code exhibits the weakest performance.

In Figure 10, the clutter is randomly distributed across distance units 20 to 100. Two strong clutter echoes are present at distance units 65 and 70, while a weak target exists at distance unit 55. After processing with the matched filter, the primary sidelobe of the clutter often exceeds the mainlobe of the target, rendering it challenging to discern weak targets near the cluttered region. Conversely, the EWMF algorithm can substantially diminish clutter sidelobes, thereby safeguarding the target's mainlobe from being obscured by dominant clutter. This increases the SINR between the target's mainlobe and the first sidelobe of the clutter from $-7$ dB to 28 dB. The distance autocorrelation varies with different transmitted waveforms, with integrated waveforms experiencing greater mainlobe loss. This is attributed to communication modulation disrupting the inherent autocorrelation of the original transmitted waveform. Optimized low-range sidelobes effectively reduce clutter interference from different range cells. Especially in complex environments, low sidelobes can suppress non-target echoes and reduce responses to surrounding clutter, thereby improving target detection accuracy and positioning precision, and preventing false alarms. At the same time, low sidelobes improve range resolution, reducing interference from nearby targets, and are particularly effective in preventing mutual interference of echo signals in multi-target detection. Furthermore, low sidelobes can increase SNR, improving the ability to extract target echoes from noise and enhancing the reliability of detection.

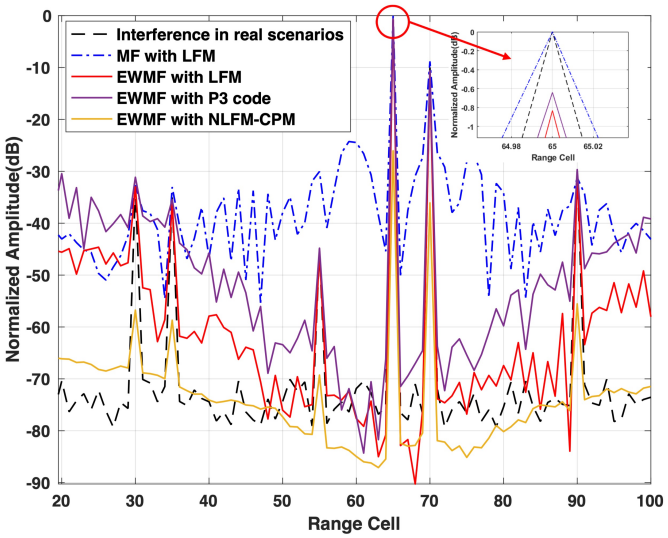



**Figure 10.** Comparison of the recognition capability of conventional matched filters and EWMF filters for weak targets under different waveform conditions.

## 5. Conclusions

In this letter, a novel NLFM-CPM radar-communication integrated waveform was designed, enabling flexible modulation of communication signals while achieving radar detection, thus meeting both communication and detection requirements. The time-domain echo signals were discretized, and the received data were rearranged to design filter coefficients based on a weighted time-domain correlation matrix. For the minimum ISL criterion, the waveform and filter were jointly optimized, with constraints on the mainlobe width and pulse compression levels. To solve the SOCP problem, the ADMM algorithm was employed, transforming the SOCP problem into a k-iteration alternating problem by introducing Lagrange multipliers. Through iterative updates of the transmitted signal and filter, an optimal solution for minimizing ISL was obtained. During the iterations, a

reference sidelobe template based on environmental design was introduced, guiding the filter coefficients to converge towards the reference template and achieving the minimum sidelobe level for the EWMF method. The LPG caused by mismatched filtering was analyzed, and its lower bound was derived using the Young inequality. Finally, the algorithm's complexity was analyzed, and its performance, along with the impact of communication modulation parameters, was validated through experimental simulation data. The results demonstrated that the EWMF algorithm effectively reduced NRSI and improved SINR for weak targets. In our forthcoming research, since it is also necessary to balance the main target signal gain and sidelobe suppression of ambiguous signals in multi-target detection, we plan to incorporate range ambiguity factors into the EWMF design of the integrated waveform.

**Author Contributions:** Conceptualization, H.W. and H.T.; methodology, H.W.; software, H.W.; validation, H.W., H.T. and T.Z.; formal analysis, H.W.; investigation, H.W.; resources, H.W.; data curation, H.W.; writing—original draft preparation, H.W.; writing—review and editing, H.W., H.T., T.Z. and W.L.; visualization, H.W.; supervision, H.T.; project administration, H.T.; funding acquisition, H.T. All authors have read and agreed to the published version of the manuscript.

**Funding:** This research was funded in part by National Key Laboratory Foundation under grant number 6142411332103 and 6142411332105, in part by Shanghai Aerospace Science and technology Innovation Foundation under grant number SAST2021, in part by National Natural Science Foundation of China under grant number 62301404, and in part by Basic Research Program of Shannxi Province under grant number 202203021212204.

**Data Availability Statement:** The data generated or analyzed during this study are not publicly available due to privacy restrictions. Requests for access to data can be directed to the corresponding author.

**Conflicts of Interest:** The authors declare no conflicts of interest.

## References

1. Dong, F.; Wang, W.; Hu, Z.; Hui, T. Low-Complexity Beamformer Design for Joint Radar and Communications Systems. *IEEE Commun. Lett.* **2021**, *25*, 259–263. [CrossRef]
2. Zhang, F.; Zhang, Z.; Yu, W.; Truong, T.-K. Joint Range and Velocity Estimation With Intrapulse and Intersubcarrier Doppler Effects for OFDM-Based RadCom Systems. *IEEE Trans. Signal Process.* **2020**, *68*, 662–675. [CrossRef]
3. Liu, Y.; Liao, G.; Xu, J.; Yang, Z.; Zhang, Y. Adaptive OFDM Integrated Radar and Communications Waveform Design Based on Information Theory. *IEEE Commun. Lett.* **2017**, *21*, 2174–2177. [CrossRef]
4. Sit, Y.L.; Nuss, B.; Zwick, T. On Mutual Interference Cancellation in a MIMO OFDM Multiuser Radar-Communication Network. *IEEE Trans. Veh. Technol.* **2018**, *67*, 3339–3348. [CrossRef]
5. Damtie, B.; Lehtinen, M.; Orispaa, M.; Vierinen, J. Mismatched Filtering of Aperiodic Quadriphase Codes. *IEEE Trans. Inf. Theory* **2008**, *54*, 1742–1749. [CrossRef]
6. Kajenski, P.J. Mismatch Filter Design via Convex Optimization. *IEEE Trans. Aerosp. Electron. Syst.* **2016**, *52*, 1587–1591. [CrossRef]
7. Ciuonzo, D.; De Maio, A.; Foglia, G.; Piezzo, M. Intrapulse Radar-Embedded Communications via Multiobjective Optimization. *IEEE Trans. Aerosp. Electron. Syst.* **2015**, *51*, 2960–2974. [CrossRef]
8. Jiang, M.; Liao, G.; Yang, Z.; Liu, Y.; Chen, Y. Tunable Filter Design for Integrated Radar and Communication Waveforms. *IEEE Commun. Lett.* **2021**, *25*, 570–573. [CrossRef]
9. Li, H.; Liu, Y.; Liao, G.; Chen, Y.; Tang, H. Complementary Mismatch Filter Group Design for Integrated Radar and Communications Waveforms Observed in Colored Noise. *IEEE Wirel. Commun. Lett.* **2023**, *12*, 227–231. [CrossRef]
10. Yu, L.; He, F.; Zhang, Y.; Su, Y. Low-PSL Mismatched Filter Design for Coherent FDA Radar Using Phase-Coded Waveform. *IEEE Geosci. Remote Sens. Lett.* **2023**, *20*, 3507405. [CrossRef]
11. Sun, Y.; Liu, Q.; Cai, J.; Long, T. A Novel Weighted Mismatched Filter for Reducing Range Sidelobes. *IEEE Trans. Aerosp. Electron. Syst.* **2019**, *55*, 1450–1460. [CrossRef]
12. Jin, L.; Wang, J.; Zhong, Y.; Wang, D. Optimal Mismatched Filter Design by Combining Convex Optimization With Circular Algorithm. *IEEE Access* **2022**, *10*, 56763–56772. [CrossRef]

13. Baden, J.M.; Cohen, M.N. Optimal Peak Sidelobe Filters for Biphase Pulse Compression. In Proceedings of the IEEE International Conference on Radar, Arlington, VA, USA, 7–10 May 1990; pp. 249–252.
14. He, X.; Hu, L.; Wu, Z.; Wu, S. Optimal Sidelobe Suppression Filters Design with a Constraint of Maximum Loss in Process Gain. In Proceedings of the IET International Radar Conference, Guilin, China, 20–22 April 2009; pp. 1–4.
15. Rihaczek, A.W.; Golden, R.M. Range Sidelobe Suppression for Barker Codes. *IEEE Trans. Aerosp. Electron. Syst.* **1971**, *AES-7*, 1087–1092. [CrossRef]
16. Wang, Z.; Liao, G.; Yang, Z. Space-Frequency Modulation Radar-Communication and Mismatched Filtering. *IEEE Access* **2018**, *6*, 24837–24845. [CrossRef]
17. Zhou, K.; Li, D.; Su, Y.; Liu, T. Joint Design of Transmit Waveform and Mismatch Filter in the Presence of Interrupted Sampling Repeater Jamming. *IEEE Signal Process. Lett.* **2020**, *27*, 1610–1614. [CrossRef]
18. Tang, Z.; Bao, Q.; Pan, J.; Dai, H.; Jiang, W. Noncooperative Bistatic Radar Countermeasures Based on the Joint Design of Radar Waveforms and Mismatched Filters. *IEEE Geosci. Remote Sens. Lett.* **2023**, *20*, 3502805. [CrossRef]
19. Davis, M.S.; Lanterman, A.D. Minimum Integrated Sidelobe Ratio Filters for MIMO Radar. *IEEE Trans. Aerosp. Electron. Syst.* **2015**, *51*, 405–416. [CrossRef]
20. Zhang, R.; Cheng, L.; Wang, S.; Lou, Y.; Gao, Y.; Wu, W. Integrated Sensing and Communication With Massive MIMO: A Unified Tensor Approach for Channel and Target Parameter Estimation. *IEEE Trans. Wirel. Commun.* **2024**, *23*, 8571–8587. [CrossRef]
21. Ma, Y.; Ma, R.; Lin, Z.; Zhang, R.; Cai, Y.; Wu, W. Improving Age of Information for Covert Communication with Time-Modulated Arrays. *IEEE Internet Things J.* **2024**, *99*, 1. [CrossRef]
22. Zhou, K.; Quan, S.; Li, D.; Liu, T.; He, F.; Su, Y. Waveform and Filter Joint Design Method for Pulse Compression Sidelobe Reduction. *IEEE Trans. Geosci. Remote Sens.* **2022**, *60*, 5107615. [CrossRef]
23. Levanon, N. Creating Sidelobe-Free Range Zone Around Detected Radar Target. In Proceedings of the IEEE 28th Convention of Electrical & Electronics Engineers in Israel (IEEEI), Eilat, Israel, 3–5 December 2014; pp. 1–5.
24. Candan, C. On the Design of Mismatched Filters with an Adjustable Matched Filtering Loss. In Proceedings of the 2010 IEEE Radar Conference, Arlington, VA, USA, 10–14 May 2010; pp. 1311–1316.
25. Kulpa, J.S. Noise Radar Sidelobe Suppression Algorithm Using Mismatched Filter Approach. *Int. J. Microw. Wirel. Technol.* **2016**, *8*, 865–869. [CrossRef]
26. Nunn, C.; Kretschmer, F.F. Performance of Pulse Compression Code and Filter Pairs Optimized for Loss and Integrated Sidelobe Level. In Proceedings of the 2007 IEEE Radar Conference, Waltham, MA, USA, 17–20 April 2007; pp. 110–115.
27. Levanon, N.; Mozeson, E. *Radar Signals*; Wiley: Hoboken, NJ, USA, 2004; pp. 20–29.
28. Bao, Z.; Xing, M.; Wang, T. *Radar Imaging Technology*; Publishing House of Electronics Industry: Beijing, China, 2005; pp. 22–24.
29. Tang, B.; Tang, J. Joint Design of Transmit Waveforms and Receive Filters for MIMO Radar Space-Time Adaptive Processing. *IEEE Trans. Signal Process.* **2016**, *64*, 4707–4722. [CrossRef]
30. Jing, Y.; Liang, J.; Tang, B.; Li, J. Designing Unimodular Sequence with Low Peak of Sidelobe Level of Local Ambiguity Function. *IEEE Trans. Aerosp. Electron. Syst.* **2019**, *55*, 1393–1406. [CrossRef]
31. Wang, F.; Pang, C.; Wu, H.; Li, Y.; Wang, X. Designing Constant Modulus Complete Complementary Sequence with High Doppler Tolerance for Simultaneous Polarimetric Radar. *IEEE Signal Process. Lett.* **2019**, *26*, 1837–1841. [CrossRef]
32. Guo, Q.; Liao, G.; Wu, Y.; Li, J. Pattern Synthesis Method for Arbitrary Arrays Based on LCMV Criterion. *Electron. Lett.* **2003**, *39*, 1628–1630. [CrossRef]
33. Kosem, T. Matrix Versions of Young's Inequality. *Math. Inequal. Appl.* **2009**, *12*, 239–254. [CrossRef]


**Disclaimer/Publisher's Note:** The statements, opinions and data contained in all publications are solely those of the individual author(s) and contributor(s) and not of MDPI and/or the editor(s). MDPI and/or the editor(s) disclaim responsibility for any injury to people or property resulting from any ideas, methods, instructions or products referred to in the content.